Available online at www.sciencedirect.com
ScienceDirect
Comput. Methods Appl. Mech. Engrg. 373 (2021) 113511
Computer methods in applied mechanics and engineering
www.elsevier.com/locate/cma

A discrete approach for modeling degraded elastic fibers in aortic dissection

Malte Rolf-Pissarczyk[a], Kewei Li[a], Dominik Fleischmann[b], Gerhard A. Holzapfel[a,c,*]

[a] *Institute of Biomechanics, Graz University of Technology, Austria*
[b] *3D and Quantitative Imaging Laboratory, Department of Radiology, Stanford University, Stanford 94305, CA, USA*
[c] *Department of Structural Engineering, Norwegian University of Science and Technology (NTNU), Trondheim, Norway*

Received 9 July 2020; received in revised form 6 October 2020; accepted 9 October 2020
Available online 2 November 2020

Abstract

The initiation and propagation of aortic dissection have not yet been fully elucidated. An essential role is attributed to the degradation of inter-lamellar elastic fibers in the aortic media which causes a significant lowering of the radial strength. Inter-lamellar elastic fibers are aligned radially and contribute mainly to the cohesion of the lamellar units in the aortic media. Computational studies that consider these pathological findings during aortic dissection are rare. In this study, we propose a constitutive model which incorporates the degeneration of inter-lamellar elastic fibers. For this purpose, the recently introduced discrete fiber dispersion model is applied to include symmetrically dispersed inter-lamellar elastic fibers in a strain–energy function. Damaged or degraded elastic fibers are excluded from the strain–energy function by introducing a degradation parameter. Subsequently, the proposed model is implemented in a finite element program and verified with two representative numerical examples, uniaxial extension and simple shear. An aortic dissection geometry with two distinct layers, motivated from patient data, is then created to study the influence of degraded radially-directed elastic fibers on the stress distribution in an aortic dissection. In summary, the presented constitutive model is able to capture the degradation of inter-lamellar elastic fibers during aortic dissection. Moreover, the finite element analysis results of the patient-data motivated geometry suggest a possible mechanism triggering the dissection propagation.

Keywords: Constitutive modeling; Discrete fiber dispersion model; Finite element analysis; Fibrous tissue; Elastic fibers; Aortic dissection

1. Introduction

The first acute type A aortic dissection was described by Frank Nicholls in 1760 [1]. He was the personal physician of George II, King of England who died due to sustained fatal cardiac tamponade caused by an aortic dissection. It is valuable to read the interesting history of aortic dissection documented by Criado [2]. It seems that Erdheim [3,4] was the first who described cystic medial necrosis of the aorta, which are focal areas of tissue destruction. Cystic medial necrosis is seen in surgical specimens of aortic dissection, and it seems to be related with higher risks of several aortic complications [5].

* Corresponding author at: Institute of Biomechanics, Graz University of Technology, Austria.
E-mail address: holzapfel@tugraz.at (G.A. Holzapfel).

https://doi.org/10.1016/j.cma.2020.113511

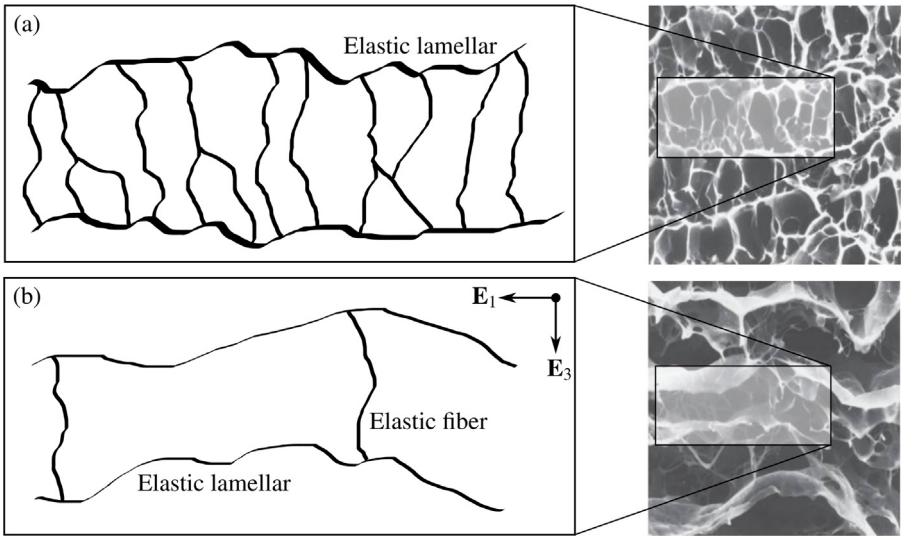

Fig. 1. 2D schematic representation of the elastic lamellar sheets within the human aortic media oriented in the circumferential direction $\mathbf{E}_1$. Interconnecting elastic fibers within the lamellar unit oriented radially ($\mathbf{E}_3$) building a 3D architecture: (a) healthy case; (b) diseased case.
Source: SEM images are reprinted from Nakashima [21].

Aortic dissection is a rare but life-threatening cardiovascular disease, which may be initiated as a small tear in the intimal (inner) layer of the aortic wall before it extends to the medial layer causing a wall separation. Subsequently, the tear propagates along the longitudinal direction of the medial layer resulting in a false lumen which may lead to vascular thrombosis. Some have hypothesized that a delamination of the medial layer caused by an intraluminal hematoma instead initiates the aortic dissection, which triggers an intimal tear at a later stage of the disease [6,7]. This controversy demonstrates that despite comprehensive studies from various research fields, a fundamental explanation of the mechanisms initiating aortic dissection remains rather unknown. Nevertheless, Humphrey [8] proposed that the predominant mechanisms can be summarized as follows: remodeling of collagen fibers, degradation of elastic fibers, local accumulation of glycosaminoglycans, and loss and re-differentiation of smooth muscle cells (SMCs). Those mechanisms are typically found in the media, but can also involve adjacent layers. Each mechanism may not be solely responsible for the initiation of an aortic dissection, but the pathological alteration of various constituents may promote the failure of the aortic wall. In many cases, the pathology of aortic dissection coincides also with age-related alterations of the aortic wall. Studies have shown however that in most cases the diseased aortic wall exhibits a more severe grade of the respective pathological alteration [9–11]. Besides, there are other cardiovascular diseases, like diseases of the bicupid aortic valve [12–14], which show a similar pathology to that found in aortic dissection.

Remarkably, Fig. 1 illustrates the healthy and diseased lamellar units of the medial layer which are arranged in parallel to the luminal surface. The lamellar unit consists of fenestrated elastic lamellar sheets and radially-directed inter-lamellar elastic fibers [15,16], which consist of amorphous elastin and microfibrils, respectively [8,17]. The arrangement of the elastic lamellar sheet and inter-lamellar elastic fibers in the healthy and dissected human medial layer is examined in some structural investigations [18–21]. Those investigations found that radially-directed inter-lamellar elastic fibers are degraded in the diseased medial layer, whereas the elastic lamellae appeared almost normal. In general, the degradation of elastic fibers in the medial layer of the aorta can be explained by either proteolytic degradation or mechanical damage. As hypothesized by Humphrey [8] and later by Cikach et al. [22], inter-lamellar elastic fibers can be mechanically damaged by an occurring (Donnan) swelling pressure between the elastic lamellae in the extracellular matrix, which may be caused by the accumulation of pooled glycosaminoglycans. This suggests a significant reduced cohesiveness of the lamellar units and the development of local inhomogeneities causing stress concentrations. In consequence, the media may be more vulnerable to shear and dissecting forces in aortic dissection due to the degradation of inter-lamellar elastic fibers.

Following the hypothesis of Humphrey [8], the influence of pooled GAGs was studied by using semi-analytical and finite element-based continuum approaches [23,24]. These computational studies documented significant intramural stress concentrations around the accumulation of GAGs when an intra-lamellar (Donnan) swelling pressure is present. Then, a particle-based computational model was proposed to study the role of pooled GAGs in the initiation and propagation of intra-lamellar delamination [25,26]. Firstly, it was shown that the activation of SMCs can prevent damage in the aortic wall, and, secondly, that the accumulation of GAGs may initiate and propagate the delamination by extending and coalescing. To the best of the authors' knowledge, there are no further computational studies which examine on the influence of pooled GAGs in aortic dissections.

Other computational studies, however, have focused on modeling the initiation and propagation of the aortic dissection. This is accomplished by using damage models or numerical techniques which deal with displacement discontinuities caused by the delamination of the aortic wall. The first study on this topic is the one proposed by Gasser and Holzapfel [27] who employed a continuum model to investigate the propagation of aortic dissection with cohesive elements in a peeling test. They treated the aortic wall as a fiber-reinforced composite with collagen fibers embedded in an isotropic ground substance. A similar approach was used by Ferrara et al. [28], as an extension to the model in Ferrara et al. [29]. These authors modeled the delamination of the aortic wall including cohesive effects. The various cohesive parameters of the model were determined by a sensitivity analysis. In contrast, Wang et al. [30] used an energy approach on the basis of the energy release rate. They modeled the initiation of the tear and its propagation with the extended finite element method [31,32], and determined a critical pressure at which the dissection starts to propagate. The propagation of aortic dissection was described by a linear traction–separation law. More recently, the computational approach of Gültekin et al. [33] modeled the propagation of the false lumen with the phase-field approach by prescribing a tear within a multi-layered segment of the aortic wall. The results of the finite element analysis demonstrated that the dissection propagation follows a helical shape along the aorta which aligns with the orientation of the collagen fibers. Moreover, the region proximal to the intimal tear was subjected to significant damage. For completeness, interested readers are referred to some universal damage models for soft tissues [34–36].

Micro-structure-based computational approaches were also employed to model the damage of individual constituents of the aortic wall. For example, in the computational study of Shah et al. [37], a macro- and micro-scale model of the aortic wall was incorporated to capture the disease-dependent damage of fibers. The micro-structure of the aortic wall was defined by a network of collagen fibers embedded in a non-fibrous matrix described by a neo-Hookean model. The failure of fibers was taken into account by applying a damage model with a failure criterion on the basis of a critical stretch threshold. They performed uniaxial and biaxial extension tests to validate the computational approach. Subsequently, Witzenburg et al. [38] extended this approach by using histological observations. They modeled the lamellar unit of the media with 2D sheets of elastic and collagen fibers, which were interconnected by SMCs and fibrillins. In contrast, Thunes et al. [39,40] proposed a structural model of the medial lamellar unit including elastic and collagen fibers to obtain a better understanding of the initiation of aortic dissection. Pal et al. [41] investigated the correlation between radially-directed collagen fibers and the delamination strength by using a predictive mechanistic model, and data from the experimental study of Pasta et al. [42]. Most recently, Yu et al. [43] published an approach to model the failure mechanics of dissection propagation on the basis on an energy failure criteria. Two medial strips were defined for a peeling test which were connected by discrete collagen fibers. Collagen fibers that exceeded the defined failure criteria were removed to model the dissection propagation. They claimed to have published the first quantitative agreement between experimental results of a peeling tests and a computational model which is based on microscopic features of the aortic constituents. The results suggest an avalanche-like failure of the aortic wall. In a follow-up study [44], they compared the contribution of elastic and collagen fibers in bonding of the aortic wall, and concluded that collagen fibers have a higher contribution to the inter-lamellar stiffness, strength and toughness.

In the present study, we assume that the elastic lamellae and the inter-lamellar elastic fibers can be accounted for by a dispersion of elastic fibers, as recently postulated by Holzapfel et al. [45]. Inter-lamellar elastic fibers are assumed to be symmetrically dispersed in the lamellar unit of the media. In general, there are two main approaches to model a dispersed fiber distribution, the generalized structural tensor approach and the angular integration (AI) approach. In the work of Li et al. [46], those two approaches were summarized, and the discrete fiber dispersion (DFD) model was introduced to formulate a strain–energy function which includes the dispersion of collagen fibers while excluding fibers under compression. The authors incorporated the fiber dispersion as a summation of a finite

number of discrete fiber contributions. In comparison with the continuous approach such as the AI method, the DFD model reduces the computational costs significantly while maintaining accuracy and allowing for the exclusion of fibers under compression [46]. In the DFD model, a unit hemisphere is first discretized into a finite number of elementary areas such as spherical triangles, and a representative fiber direction at the centroid of each spherical triangle is computed. A discrete fiber density for each representative fiber direction is then determined by numerical integration of the continuous fiber probability density function (PDF) over the corresponding elementary area. The accuracy of the integration depends strongly on the number of elementary areas. In this study, we use the DFD model to account for the dispersion of elastic fibers in the medial layer of the aortic wall. Moreover, we introduce a degradation parameter which excludes damaged or degraded elastic fibers from the strain–energy function to model the degradation of radially-directed elastic fibers. The degradation initiates from the radial direction due to the highest occurring stretch.

The outline of this study is as follows. In Section 2, we present the continuum mechanical framework of the constitutive model incorporating the degradation of elastic fibers. Briefly, the explicit form of the strain–energy function, the Cauchy stress and the elasticity tensors are formulated in a decoupled form, as needed for the implementation in a finite element code. In Section 3, we demonstrate the performance of the constitutive model with two representative numerical examples by using the finite element analysis program FEAP [47]. Subsequently, we construct the geometry of an acute aortic dissection, motivated from patient data, with the commercial finite element analysis program Abaqus/Standard [48] to model the aortic dissection. Finally, the proposed constitutive model and the obtained computational results are discussed in Section 4, which is followed by suggestions for future studies.

2. Degradation of elastic fibers

In this section, the continuum mechanical framework which incorporates the degradation of elastic fibers during aortic dissection is presented. In addition, we describe the kinematics in order to formulate the strain–energy function and the corresponding Cauchy stress and elasticity tensors.

2.1. Kinematics

The deformation map $\boldsymbol{\chi}$ of a material point $\mathbf{X}$ located in the (undeformed) reference configuration $\mathcal{B}_0$ to a spatial point $\mathbf{x}$ in the (deformed) current configuration $\mathcal{B}$ is defined as $\mathbf{x} = \boldsymbol{\chi}(\mathbf{X})$. To characterize the local deformation at a material point, the deformation gradient $\mathbf{F}(\mathbf{X})$ is formulated as $\mathbf{F}(\mathbf{X}) = \partial\boldsymbol{\chi}(\mathbf{X})/\partial\mathbf{X}$. This relation allows us to formulate the map of the infinitesimal line element $\mathrm{d}\mathbf{X}$ from the reference to the current configuration as $\mathrm{d}\mathbf{x} = \mathbf{F}\mathrm{d}\mathbf{X}$. We assume here an incompressible material so that the determinant of the deformation gradient $J = \det\mathbf{F}(\mathbf{X}) > 0$, or Jacobian, is always $J \equiv 1$. Thus, we follow the multiplicative decomposition of the deformation gradient [49,50], and decouple the deformation gradient $\mathbf{F}$ into a volumetric (dilatational) part $J^{1/3}\mathbf{I}$ and an isochoric (distortional) part $\overline{\mathbf{F}} = J^{-1/3}\mathbf{F}$, where $\mathbf{I}$ denotes the second-order unit tensor. The symmetric right Cauchy–Green tensor, representing a deformation measure in the reference configuration, and its modified counterpart is then given by $\mathbf{C} = \mathbf{F}^{\mathrm{T}}\mathbf{F}$ and $\overline{\mathbf{C}} = \overline{\mathbf{F}}^{\mathrm{T}}\overline{\mathbf{F}}$, respectively, while the symmetric left Cauchy–Green tensor, related to the current configuration, and its modified counterpart is provided by $\mathbf{b} = \mathbf{F}\mathbf{F}^{\mathrm{T}}$ and $\overline{\mathbf{b}} = \overline{\mathbf{F}}\,\overline{\mathbf{F}}^{\mathrm{T}}$, respectively. Then, the first invariant I_1 and its modified counterpart $\bar{I}_1$ are defined as

$$I_1 = \mathrm{tr}\mathbf{C} = \mathrm{tr}\mathbf{b}, \qquad \bar{I}_1 = \mathrm{tr}\overline{\mathbf{C}} = \mathrm{tr}\overline{\mathbf{b}}. \tag{1}$$

We further introduce the fourth invariant I_4 and its modified counterpart $\bar{I}_4$ as

$$I_4 = \mathbf{C}\colon \mathbf{N}\otimes\mathbf{N} = \mathbf{n}\otimes\mathbf{n}, \qquad \bar{I}_4 = \overline{\mathbf{C}}\colon \mathbf{N}\otimes\mathbf{N} = \overline{\mathbf{n}}\otimes\overline{\mathbf{n}}, \tag{2}$$

where I_4 represents the squared fiber stretch in a direction $\mathbf{N}$, where $\mathbf{N}$ is defined in the reference configuration, while $\mathbf{n} = \mathbf{F}\mathbf{N}$ and $\overline{\mathbf{n}} = \overline{\mathbf{F}}\mathbf{N}$ define the related directions in the current configuration. The direction $\mathbf{N}$ of a fiber can be expressed by the polar angle Θ and the azimuth angle Φ so that we may write

$$\mathbf{N} = \sin\Theta\cos\Phi\mathbf{E}_1 + \sin\Theta\sin\Phi\mathbf{E}_2 + \cos\Theta\mathbf{E}_3, \tag{3}$$

where $\mathbf{E}_i$, $i = 1, 2, 3$, are the unit Cartesian basis vectors.

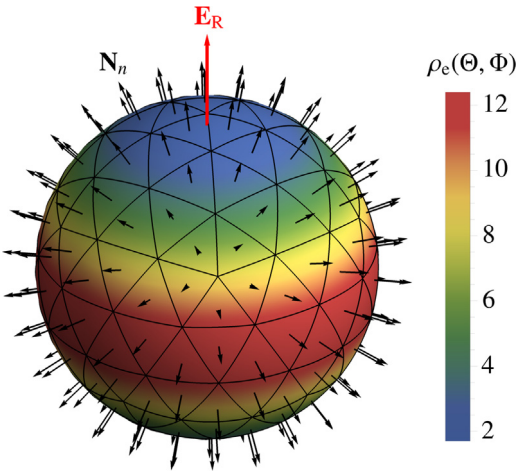

Fig. 2. PDF of elastic fibers ρ_e represented by a von Mises distribution (7) with the radial vector $\mathbf{E}_R$ and the concentration parameter $b_e = 1$, mapped on the unit hemisphere. The unit hemisphere is discretized with $2m$ representative fiber directions $\mathbf{N}_n$, $n = 1, \ldots, m$, (black arrows) defined at the centroid of the respective spherical triangle.

2.2. Strain–energy function Ψ

We postulate a strain–energy function Ψ, or Helmholtz free-energy function, per unit reference volume, which represents the passive material behavior of the aortic wall. The active material behavior generated by the SMCs is neglected in this study. For the sake of computational efficiency, the strain–energy function is decoupled as

$$\Psi = \Psi_{\text{vol}} + \Psi_{\text{iso}}, \tag{4}$$

where Ψ_{vol} and Ψ_{iso} represent the purely volumetric part and the isochoric part of the deformation, respectively [51]. We define the volumetric part as

$$\Psi_{\text{vol}} = \frac{K}{4}(J^2 - 1 - 2\ln J), \tag{5}$$

where K is the bulk modulus, which is a penalty parameter to enforce the kinematic incompressibility constraint. The isochoric part, which represents the respective constituents of the aortic wall, namely the ground substance Ψ_g, the collagen fibers Ψ_c and the elastic fibers Ψ_e, is decomposed as

$$\Psi_{\text{iso}} = \Psi_g + \Psi_c + \Psi_e. \tag{6}$$

As illustrated in Fig. 1, we assume that the elastic fibers in the elastic lamellae, and the inter-lamellar elastic fibers can be accounted for as a dispersion of elastic fibers. For this purpose, the DFD model [46] was used to describe all the elastic fibers as dispersed between the elastic lamellae. The rotationally symmetric fiber dispersion is represented by an integrable PDF $\rho_e(\Theta, \Phi)$, which is defined over the unit hemisphere as $\mathbb{S} = \{(\Theta, \Phi) | \Theta \in [0, \pi], \Phi \in [0, \pi]\}$. We define the PDF of elastic fibers by a von Mises distribution of the form

$$\rho_e(\Theta, \Phi) = 4\sqrt{\frac{b_e}{2\pi}} \frac{\exp\left[-2b_e(\mathbf{N} \cdot \mathbf{E}_R)^2\right]}{\text{erf}\left(\sqrt{2b_e}\right)}, \tag{7}$$

where $\text{erf}(x)$ denotes the standard error function, and b_e represents the concentration parameter of elastic fibers, which describes a symmetric dispersion with respect to the radial vector $\mathbf{E}_R$. Generally, $\mathbf{E}_R$ does not coincide with the Cartesian axis $\mathbf{E}_3$. A representative illustration of the symmetric fiber PDF mapped on a unit sphere is shown in Fig. 2.

Fig. 2 shows the discretization of the unit sphere into a finite number of elementary areas $\Delta\mathbb{S}_n$, $n = 1, \ldots, m$ [46,52], which can be physically interpreted as the normalized number of fibers within the respective elementary area. Here, we chose a spherical triangle as the elementary area for the discretization. At the centroid of each elementary area we define a discrete fiber angle (Θ, Φ) which represents all the fibers distributed within

the elementary area. Because of symmetry, we only need to discretize half of the unit sphere. After discretizing the unit hemisphere into m elementary areas, we formulate the discrete density ρ_{en} of elastic fibers as

$$\rho_{en} = \frac{1}{2\pi} \int_{\Delta \mathbb{S}_n} \rho_e(\Theta, \Phi) \sin\Theta \mathrm{d}\Theta \mathrm{d}\Phi, \qquad n = 1, \ldots, m. \tag{8}$$

We further have to fulfill the normalization condition which is by definition satisfied by the choice of (7). For the discrete approach, we then rewrite the normalization condition over the unit hemisphere with (8), i.e.

$$\sum_{n=1}^{m} \rho_{en} = 1. \tag{9}$$

Following the DFD model, the total strain–energy function of elastic fibers Ψ_e in the reference configuration can then be written in the discrete form as

$$\Psi_e = \sum_{n=1}^{m} \rho_{en} \Psi_{en}(\bar{\lambda}_{en}^2), \tag{10}$$

where $\Psi_{en}(\bar{\lambda}_{en}^2)$ represents the strain–energy function associated with the fiber direction $\mathbf{N}_n$ of the elementary area n. A single elastic fiber is treated similarly to a 1D element which bears load only in the direction of the fiber. Therefore, $\Psi_{en}(\bar{\lambda}_{en}^2)$ depends solely on the squared fiber stretch $\bar{\lambda}_{en}^2 = \bar{I}_{4n} = \bar{\mathbf{C}} : \mathbf{N}_n \otimes \mathbf{N}_n$, also known as the true fiber stretch [52], which implies that the fiber recruitment stretch is neglected. This is motivated by the observation of different studies suggesting that elastic fibers in the aortic wall are always under tension [53]. We further assume that elastic fibers contribute to the strain–energy function only when they are under tension due to the wavy structure of fibers in the aortic wall [54]. In addition, the fiber strain–energy function has also to satisfy

$$\Psi_{en}(1) = 0 \quad \text{and} \quad \Psi'_{en}(1) = 0. \tag{11}$$

Subsequently, we introduce a degradation parameter $\xi \in [0, 1]$ to describe the damage of elastic fibers as a result of the separation of the elastic lamellae, as illustrated in Fig. 1. In analogy to the continuum damage theory [51], we define

$$\xi = \begin{cases} 0 & \text{healthy,} \\ 1 & \text{completely diseased (damaged/degraded).} \end{cases}$$

We further define a degradation or critical fiber angle $\Theta_\xi = \pi\xi/2$ to exclude elastic fibers from the total strain–energy function, i.e.

$$\Psi_{en} = \begin{cases} f_{en}(\bar{\lambda}_{en}^2) & \text{if} \quad \Theta_n \geq \Theta_\xi \quad \text{and} \quad \lambda_{en}^2 \geq 1, \\ 0 & \text{else,} \end{cases} \tag{12}$$

where f_{en} represents a mathematical expression of the strain–energy function of a single elastic fiber. As shown in Fig. 3, we exclude the elastic fiber from the total strain–energy function, which we interpret as diseased (damaged/degraded), when the discrete fiber angle Θ_n is smaller than a critical fiber angle Θ_ξ (Fig. 3). This is motivated by the fact that elastic fibers aligned in the radial direction undergo the highest stretch under diseased conditions, and, therefore, are more prone to rupture. As indicated above, the pathology of aortic dissection demonstrates, inter alia, that the lamellar units are separated by a possible accumulation of GAGs which in turn is similar to a delamination force acting on the lamellar units. This delamination force may act predominately in the radial direction causing damage or degradation of elastic fibers. Thus, the definition of a critical fiber angle may be a valid assumption. The critical fiber angle Θ_ξ depends on the stage of the aortic dissection. It increases as the disease progresses. Note that we refrain here from introducing a physically-based evolution law of the elastic fiber degradation due to the lack of knowledge about the complex nature of tissue degradation in aortic dissection. A possible evolution law might be influenced by purely mechanical factors, but also by biochemical processes, triggered by age- or disease-related factors, or pathological alterations in the blood flow. This makes it challenging to use a physically-based evolution law.

Next, we define the strain–energy function of a single family of collagen fibers Ψ_c in terms of the DFD model, as formulated in Li et al. [46], i.e.

$$\Psi_c = \sum_{n=1}^{m} \rho_{cn} \Psi_{cn}(\bar{\lambda}_{cn}^2), \tag{13}$$

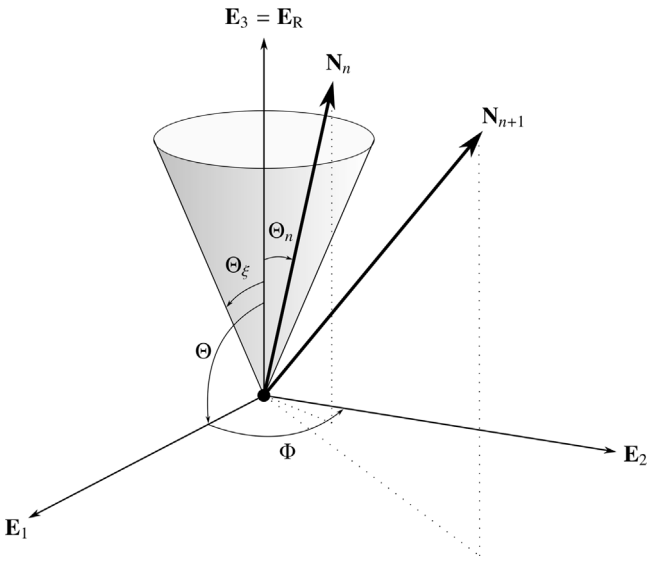

Fig. 3. Exclusion of damaged/degraded elastic fibers defined by the critical fiber angle Θ_ξ: elastic fibers distributed outside the cone, such as $\mathbf{N}_{n+1}$, are excluded from the strain–energy function, whereas elastic fibers distributed inside the cone, such as $\mathbf{N}_n$ with the discrete fiber angle Θ_n, are included. $\mathbf{E}_1, \mathbf{E}_2$ and $\mathbf{E}_3$ represent the unit Cartesian basis vectors in the circumferential, axial and radial directions, respectively.

where ρ_{cn} defines the discrete density of collagen fibers, which is expressed by

$$\rho_{\mathrm{cn}} = \frac{1}{2\pi} \int_{\Delta\mathbb{S}_n} \rho_{\mathrm{c}}(\Theta, \Phi) \sin\Theta \mathrm{d}\Theta \mathrm{d}\Phi, \qquad n = 1, \ldots, m. \tag{14}$$

Furthermore, we define the PDF of collagen fibers by a von Mises distribution of the form

$$\rho_{\mathrm{c}}(\Theta, \Phi) = 4\sqrt{\frac{b_{\mathrm{c}}}{2\pi}} \frac{\exp[2b_{\mathrm{e}}(\mathbf{N} \cdot \mathbf{E}_{\mathrm{M}})^2]}{\mathrm{erfi}\left(\sqrt{2b_{\mathrm{c}}}\right)}, \tag{15}$$

where the collagen fiber distribution around the mean fiber direction $\mathbf{E}_{\mathrm{M}}$ is described by the concentration parameter b_{c}, and $\mathrm{erfi}(x) = -\mathrm{ierf}(\mathrm{i}x)$ denotes the imaginary error function. Note that an additional family of fibers with specific material and structural parameters can be additively augmented [55].

Recently, we demonstrated the importance of considering the recruitment stretch of collagen fibers [52]. The model approach therein is based on the observation that collagen fibers are often found crimped in the unloaded configuration. Therefore, we assume that collagen fibers contribute only to the material response when straightened [54]. This approach allows a smooth transition in the fiber stretch versus stretch curve from the wavy or crimped fiber state to the straightened state. To exclude all discrete fibers under compression and crimped fibers within a dispersion, the strain–energy function of a single collagen fiber is constrained by

$$\Psi_{\mathrm{cn}}(\bar{\lambda}^2_{\mathrm{cn}}) = \begin{cases} f_{\mathrm{c}}(\bar{\lambda}^2_{\mathrm{cn}}) & \text{if } \lambda^2_{\mathrm{cn}} \geq 1, \\ 0 & \text{if } \lambda^2_{\mathrm{cn}} < 1, \end{cases} \tag{16}$$

where the squared true fiber stretch $\bar{\lambda}^2_{\mathrm{cn}}$ is given by

$$\bar{\lambda}^2_{\mathrm{cn}} = \bar{\lambda}^2_{\mathrm{c}f} / \lambda^2_{\mathrm{cr}}. \tag{17}$$

The parameter $\bar{\lambda}^2_{\mathrm{c}f} = \bar{I}_{4n} = \overline{\mathbf{C}} : \mathbf{N}_n \otimes \mathbf{N}_n$ represents the current fiber stretch of collagen fibers, while $\bar{\lambda}_{\mathrm{cr}}$ represents the critical fiber recruitment stretch that is defined as the stretch at which the fiber becomes straightened but it does not bear any load [56]. By definition, $\bar{\lambda}_{\mathrm{cr}}$ is a material parameter. We specified a constant recruitment stretch for all collagen fibers [52], and refer to Weisbecker et al. [57] for a computational approach to model a dispersed recruitment stretch.

Finally, the isochoric part of the strain–energy function including the explicit expressions for the respective constituents of the aortic wall is formulated as

$$\Psi_{\text{iso}} = \Psi_{\text{g}}(\bar{I}_1) + \sum_{n=1}^{m} \rho_{\text{c}n}\, \Psi_{\text{c}n}(\bar{\lambda}^2_{\text{c}n}) + \sum_{n=1}^{m} \rho_{\text{e}n}\, \Psi_{\text{e}n}(\bar{\lambda}^2_{\text{e}n}). \tag{18}$$

The ground substance is given by the (isotropic) neo-Hookean model, which depends on the first invariant $\bar{I}_1$ only, i.e.

$$\Psi_{\text{g}}(\bar{I}_1) = \frac{\mu}{2}(\bar{I}_1 - 3), \tag{19}$$

where the constant μ (> 0) represents the shear modulus with the dimension of stress.

In summary, we have presented the specific form of the total strain–energy function by introducing an additive decomposition into a volumetric and an isochoric part. Note that we neglected the implementation of a viscoelastic material behavior in the model framework due to insufficient experimental and theoretical evidences. The implementation of the material model into a finite element analysis program requires the determination of the Cauchy stress tensor and the elasticity tensor. In the following, only the derivation of the isochoric parts is presented. For a comprehensive description the interested reader is referred to [51,58].

2.3. Cauchy stress tensor

We differentiate the isochoric strain–energy function (18) with respect to $\overline{\mathbf{C}}/2$ to identify the fictitious second Piola–Kirchhoff stress tensor $\overline{\mathbf{S}}$, i.e.

$$\overline{\mathbf{S}} = 2\frac{\partial\, \Psi_{\text{iso}}}{\partial \overline{\mathbf{C}}} = 2\psi'_{\text{g}}(\bar{I}_1)\mathbf{I} + 2\sum_{n=1}^{m} \rho_{\text{c}n}\overline{\mathbf{S}}_{\text{c}n} + 2\sum_{n=1}^{m} \rho_{\text{e}n}\overline{\mathbf{S}}_{\text{e}n}, \tag{20}$$

where $\psi'_{\text{g}}(\bar{I}) = \partial\, \Psi_{\text{g}}(\bar{I}_1)/\partial \bar{I}_1$. The fictitious second Piola–Kirchhoff stress tensors for single collagen and elastic fibers are denoted by $\overline{\mathbf{S}}_{\text{c}n}$ and $\overline{\mathbf{S}}_{\text{e}n}$, respectively. In analogy to Li et al. [46], we formulate

$$\overline{\mathbf{S}}_{\text{c}n} = \begin{cases} \lambda_{\text{cr}}^{-2} f'_{\text{c}}(\bar{\lambda}^2_{\text{c}n})\mathbf{N}_n \otimes \mathbf{N}_n & \text{if} \quad \lambda^2_{\text{c}n} \geq 1, \\ 0 & \text{if} \quad \lambda^2_{\text{c}n} < 1, \end{cases} \tag{21}$$

and

$$\overline{\mathbf{S}}_{\text{e}n} = \begin{cases} f'_{\text{e}}(\bar{\lambda}^2_{\text{e}n})\mathbf{N}_n \otimes \mathbf{N}_n & \text{if} \quad \Theta_n \geq \Theta_\xi \quad \text{and} \quad \lambda^2_{\text{e}n} \geq 1, \\ 0 & \text{else}, \end{cases} \tag{22}$$

where $f'_{\text{c}}(\bar{\lambda}^2_{\text{c}n}) = \partial f_{\text{c}}(\bar{\lambda}^2_{\text{c}n})/\partial \bar{\lambda}^2_{\text{c}n}$ and $f'_{\text{e}}(\bar{\lambda}^2_{\text{e}n}) = \partial f_{\text{e}}(\bar{\lambda}^2_{\text{e}n})/\partial \bar{\lambda}^2_{\text{e}n}$. Applying the push-forward to (20) gives the fictitious Cauchy stress tensor $\overline{\boldsymbol{\sigma}}$. Hence,

$$\overline{\boldsymbol{\sigma}} = J^{-1}\overline{\mathbf{F}}\,\overline{\mathbf{S}}\,\overline{\mathbf{F}}^{\text{T}} = 2J^{-1}\left(\psi'_{\text{g}}(\bar{I}_1)\overline{\mathbf{b}} + \sum_{n=1}^{m} \rho_{\text{c}n}\overline{\boldsymbol{\sigma}}_{\text{c}n} + \sum_{n=1}^{m} \rho_{\text{e}n}\overline{\boldsymbol{\sigma}}_{\text{e}n}\right), \tag{23}$$

with

$$\overline{\boldsymbol{\sigma}}_{\text{c}n} = \begin{cases} \lambda_{\text{cr}}^{-2} f'_{\text{c}}(\bar{\lambda}^2_{\text{c}n})\overline{\mathbf{n}}_n \otimes \overline{\mathbf{n}}_n & \text{if} \quad \lambda^2_{\text{c}n} \geq 1, \\ 0 & \text{if} \quad \lambda^2_{\text{c}n} < 1, \end{cases} \tag{24}$$

and

$$\overline{\boldsymbol{\sigma}}_{\text{e}n} = \begin{cases} f'_{\text{e}}(\bar{\lambda}^2_{\text{e}n})\overline{\mathbf{n}}_n \otimes \overline{\mathbf{n}}_n & \text{if} \quad \Theta_n \geq \Theta_\xi \quad \text{and} \quad \lambda^2_{\text{e}n} \geq 1, \\ 0 & \text{else}, \end{cases} \tag{25}$$

where $\overline{\mathbf{n}}_n = \overline{\mathbf{F}}\mathbf{N}_n$. Next let us introduce the fourth-order projection tensor $\mathbb{P} = \mathbb{I} - \frac{1}{3}\mathbf{I} \otimes \mathbf{I}$ furnishing the physically correct deviator in the Eulerian description. Then, the double dot product of the projection tensor and the fictitious Cauchy stress tensor provides the isochoric Cauchy stress tensor, i.e.

$$\boldsymbol{\sigma}_{\text{iso}} = \mathbb{P} : \overline{\boldsymbol{\sigma}}, \tag{26}$$

where $\mathbb{I}$ denotes the symmetric fourth-order identity tensor, which can be represented by recalling the definition of the Kronecker delta δ_{ad} in component notation, i.e. $(\mathbb{I})_{abcd} = \frac{1}{2}(\delta_{ac}\delta_{bd} + \delta_{ad}\delta_{bc})$.

2.4. Elasticity tensor

We formulate the fourth-order fictitious elasticity tensor $\overline{\mathbb{C}}$ in the Lagrangian description by differentiating the fictitious second Piola–Kirchhoff stress tensor $\overline{\mathbf{S}}$ with respect to $\overline{\mathbf{C}}/2$, and, subsequently, multiply it with the factor $J^{-4/3}$, so that we obtain

$$\overline{\mathbb{C}} = 2J^{-4/3}\frac{\partial \overline{\mathbf{S}}}{\partial \overline{\mathbf{C}}} = 4J^{-4/3}\left(\psi_{\mathrm{g}}''(\bar{I}_1)\mathbf{I}\otimes\mathbf{I} + \sum_{n=1}^{m}\rho_{\mathrm{c}n}\overline{\mathbb{C}}_{\mathrm{c}n} + \sum_{n=1}^{m}\rho_{\mathrm{e}n}\overline{\mathbb{C}}_{\mathrm{e}n}\right), \tag{27}$$

with

$$\overline{\mathbb{C}}_{\mathrm{cn}} = \begin{cases} \lambda_{\mathrm{cr}}^{-4} f_{\mathrm{c}}''(\bar{\lambda}_{\mathrm{c}n}^2)\mathbf{N}_n\otimes\mathbf{N}_n\otimes\mathbf{N}_n\otimes\mathbf{N}_n & \text{if} \quad \lambda_{\mathrm{c}n}^2 \geq 1, \\ 0 & \text{if} \quad \lambda_{\mathrm{c}n}^2 < 1, \end{cases} \tag{28}$$

$$\overline{\mathbb{C}}_{\mathrm{e}n} = \begin{cases} f_{\mathrm{e}}''(\bar{\lambda}_{\mathrm{e}n}^2)\mathbf{N}_n\otimes\mathbf{N}_n\otimes\mathbf{N}_n\otimes\mathbf{N}_n & \text{if} \quad \Theta_n \geq \Theta_\xi \quad \text{and} \quad \lambda_{\mathrm{e}n}^2 \geq 1, \\ 0 & \text{else}, \end{cases} \tag{29}$$

where

$$\psi_{\mathrm{g}}''(\bar{I}_1) = \frac{\partial^2 \Psi_{\mathrm{g}}(\bar{I}_1)}{\partial \bar{I}_1 \partial \bar{I}_1}, \qquad f_{\mathrm{c}}''(\bar{\lambda}_{\mathrm{c}n}^2) = \frac{\partial^2 f_{\mathrm{c}}(\bar{\lambda}_{\mathrm{c}n}^2)}{\partial \bar{\lambda}_{\mathrm{c}n}^2 \partial \bar{\lambda}_{\mathrm{c}n}^2}, \qquad f_{\mathrm{e}}''(\bar{\lambda}_{\mathrm{e}n}^2) = \frac{\partial^2 f_{\mathrm{e}}(\bar{\lambda}_{\mathrm{e}n}^2)}{\partial \bar{\lambda}_{\mathrm{e}n}^2 \partial \bar{\lambda}_{\mathrm{e}n}^2}. \tag{30}$$

The fictitious elasticity tensor $\overline{\mathbb{C}}$ in the Eulerian description is then obtained by applying the push-forward to (27), which results in

$$\overline{\mathbb{C}} = 4J^{-1}\sum_{n=1}^{m}\rho_{\mathrm{c}n}\overline{\mathbb{C}}_{\mathrm{c}n} + 4J^{-1}\sum_{n=1}^{m}\rho_{\mathrm{e}n}\overline{\mathbb{C}}_{\mathrm{e}n} \tag{31}$$

with

$$\overline{\mathbb{C}}_{\mathrm{cn}} = \begin{cases} \lambda_{\mathrm{cr}}^{-4} f_{\mathrm{c}}''(\bar{\lambda}_{\mathrm{c}n}^2)\overline{\mathbf{n}}_n\otimes\overline{\mathbf{n}}_n\otimes\overline{\mathbf{n}}_n\otimes\overline{\mathbf{n}}_n & \text{if} \quad \lambda_{\mathrm{c}n}^2 \geq 1 \\ 0 & \text{if} \quad \lambda_{\mathrm{c}n}^2 < 1, \end{cases} \tag{32}$$

$$\overline{\mathbb{C}}_{\mathrm{e}n} = \begin{cases} f_{\mathrm{e}}''(\bar{\lambda}_{\mathrm{e}n}^2)\overline{\mathbf{n}}_n\otimes\overline{\mathbf{n}}_n\otimes\overline{\mathbf{n}}_n\otimes\overline{\mathbf{n}}_n & \text{if} \quad \Theta_n \geq \Theta_\xi \quad \text{and} \quad \lambda_{\mathrm{e}n}^2 \geq 1, \\ 0 & \text{else}. \end{cases} \tag{33}$$

Note that the term associated with the ground substance vanishes because the second derivative of the neo-Hookean model leads to $\psi_{\mathrm{g}}''(\bar{I}_1) = 0$. Following on, the isochoric elasticity tensor $\mathbb{C}_{\mathrm{iso}}$ is then obtained from (31), as defined in Holzapfel [51],

$$\mathbb{C}_{\mathrm{iso}} = \mathbb{P}\colon\overline{\mathbb{C}}\colon\mathbb{P} + \frac{2}{3}\mathrm{tr}(\overline{\boldsymbol{\sigma}})\mathbb{P} - \frac{2}{3}(\boldsymbol{\sigma}_{\mathrm{iso}}\otimes\mathbf{I} + \mathbf{I}\otimes\boldsymbol{\sigma}_{\mathrm{iso}}). \tag{34}$$

3. Representative numerical examples

We have implemented the proposed constitutive model at the Gauss-point level in the finite element analysis program FEAP [47] with the aim of demonstrating its performance by some representative numerical examples, such as uniaxial extension and simple shear of a unit cube. Subsequently, we implemented the model into the commercial finite element analysis program Abaqus/Standard [48] through a user-defined material subroutine (UMAT). Thus, it allowed us to apply the proposed constitutive model to an (acute) aortic dissection geometry motivated from patient data.

3.1. Computational studies on a single elastic lamella

The geometry of the first example is a unit cube which is discretized by a single 8-node hexadedral mixed $Q1/P0$ element, and subsequently solved by the Newton–Raphson method. The augmented Lagrangian method in FEAP [47], as described in Simo and Taylor [59], was applied to ensure incompressibility. For these numerical examples we reduced the isochoric part of the strain–energy function to the part associated with elastic fibers. We verified the implementation by comparing the analytical or theoretical solution, which was computed in MATLAB [60], with the numerical results obtained by FEAP [47]. The material parameters of the elastic fibers were determined by fitting the constitutive model to experimental data obtained from the study of Matsumoto et al. [61].

3.1.1. Identification of constitutive parameters

The experimental study of Matsumoto et al. [61] describes the uniaxial extension test of a single elastic lamella from a porcine aorta with a thickness of $\sim 10\,\mu\text{m}$. The elastic lamella was excised from the surrounding tissue and, subsequently, the remaining tissue was removed by an enzymatic digestion with purified collagenase. Following the sample preparation, a stretch of approximately $\lambda = 3.24$ was applied on the elastic lamella to obtain the stress–stretch ratio curves. The cross-section of the samples was measured in the stress-free reference state.

We propose that the strain–energy function of a single elastic fiber $f_{\text{e}}(\bar{I}_4)$ takes on the form

$$f_{\text{e}}(\bar{I}_4) = \frac{c_1}{c_2}(\bar{I}_4^{c_2/2} - 1) - c_1 \ln \bar{I}_4^{1/2}, \tag{35}$$

where c_1 and c_2 represent material parameters. It was shown that $f_{\text{e}}(\bar{I}_4)$ fulfills the condition of a stress-free reference state and satisfies the condition of polyconvexity [62]. The constitutive parameters were determined by minimizing an objective function via nonlinear least-square analysis. The objective function is defined as the sum of the squared differences between the analytically predicted Cauchy stress σ_i and the experimental measured values $\tilde{\sigma}_i$ over the number of experimental data points N, i.e.,

$$\min_{\{c_1,c_2\}} \sum_{i=1}^{N} (\sigma_i - \tilde{\sigma}_i)^2. \tag{36}$$

We implemented the proposed strain–energy function of a single elastic fiber in Matlab [60] to obtain the analytical solution of the Cauchy stress for the uniaxial extension and simple shear test. Then, the built-in function *lsqnonlin* was used to solve the described minimization problem, and the material parameters $c_1 = 56.594\,\text{kPa}$ and $c_2 = 3.89$ were identified.

3.1.2. Uniaxial extension test

In the present example, we consider a uniaxial extension test of an incompressible unit cube with the geometry $1 \times 1 \times 1\,\text{mm}$ composed of one single hexahedral element, as shown in Fig. 4. The faces of the unit cube are aligned with the unit Cartesian basis vectors $\mathbf{E}_1, \mathbf{E}_2$ and $\mathbf{E}_3$. On the top face of the unit cube, we apply a displacement boundary condition and specify that the loading direction coincide with the radial vector $\mathbf{E}_{\text{R}} = \mathbf{E}_3$. Defined by the radial vector, a rotational symmetric dispersion of one family of elastic fibers is assumed to demonstrate the performance of the proposed constitutive model. Due to symmetry, the deformation gradient for this problem is

$$[\mathbf{F}] = \text{diag}[\lambda^{-1/2}, \lambda^{-1/2}, \lambda], \tag{37}$$

where λ represents the stretch in the $\mathbf{E}_3$-direction. In analogy, for any fiber direction $\mathbf{N}$ within the half sphere, $I_4(\mathbf{N})$ is given by

$$I_4(\mathbf{N}) = \lambda^{-1} \sin^2 \Theta + \lambda^2 \cos^2 \Theta. \tag{38}$$

Note that $I_4(\mathbf{N})$ is independent of Φ for this particular case. Then, the Cauchy stress tensor $\boldsymbol{\sigma}$ over the integration domain $\Omega = \{(\Theta, \Phi) | \Theta \in [0, \pi/2], \Phi \in [0, 2\pi], I_4 > 1\}$ of a half sphere, when the fiber dispersion is treated continuously, is

$$\boldsymbol{\sigma} = -p\mathbf{I} + \frac{c_1}{\pi} \int_{\Omega} \rho_{\text{e}}(\Theta, \Phi) I_4^{-1} (I_4^{c_2/2} - 1) \sin\Theta \mathbf{n} \otimes \mathbf{n} \text{d}\Theta \text{d}\Phi, \tag{39}$$

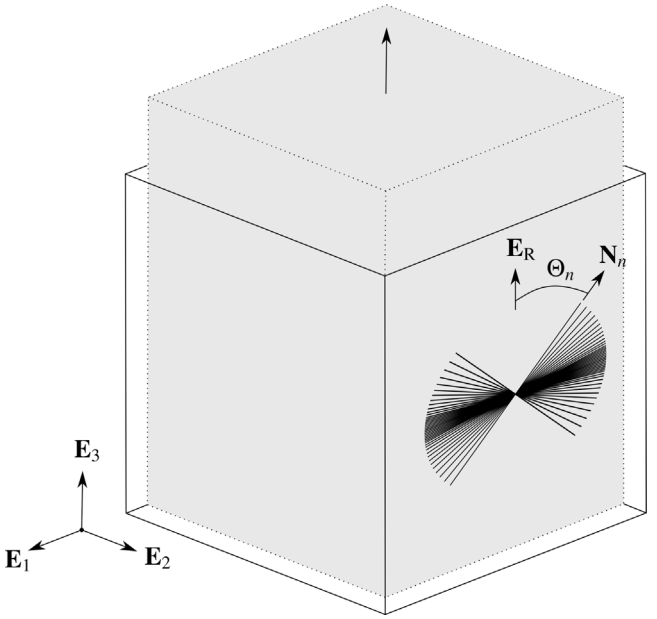

Fig. 4. Reference and intermediate configurations of a unit cube with a rotationally symmetric dispersion of elastic fibers for uniaxial extension. Radial vector $\mathbf{E}_\mathrm{R}$ is aligned with the $\mathbf{E}_3$-direction in the reference configuration. On the $(\mathbf{E}_1, \mathbf{E}_3)$-plane the cross-section of the 3D fiber dispersion including an arbitrary fiber direction $\mathbf{N}_n$ is shown.

where p represents the Lagrange multiplier to ensure incompressibility. For this case, $\rho_\mathrm{e}(\Theta, \Phi)$ reduces to

$$\rho_\mathrm{e}(\Theta) = 4\sqrt{\frac{b_\mathrm{e}}{2\pi}}\frac{\exp\left(-2b_\mathrm{e}\cos^2\Theta\right)}{\mathrm{erf}\left(\sqrt{2b_\mathrm{e}}\right)}. \tag{40}$$

Following Li et al. [55], the uniaxial Cauchy stress $\sigma \equiv \sigma_{33}$ in the $\mathbf{E}_3$-direction is expressed by

$$\sigma = \alpha\lambda^2 - \beta\lambda^{-1}, \tag{41}$$

where α and β are defined over the domain $\Sigma = \{\Theta \in [0, \pi/2] \mid I_4 > 1\}$ as

$$\alpha = 2c_1 \int_\Sigma \rho_\mathrm{e}(\Theta) I_4^{-1}(I_4^{c_2/2} - 1)\sin\Theta\cos^2\Theta \mathrm{d}\Theta, \tag{42}$$

$$\beta = c_1 \int_\Sigma \rho_\mathrm{e}(\Theta) I_4^{-1}(I_4^{c_2/2} - 1)\sin^3\Theta \mathrm{d}\Theta. \tag{43}$$

The numerical integrations of the coefficients α and β were evaluated in Matlab [60] with the built-in function *quadgk* using the adaptive Gauss–Kronrod quadrature method to verify the finite element solution of this problem by using the DFD model [63]. The material parameters c_1 and c_2 were determined in Section 3.1.1. To demonstrate the performance of the constitutive model, the concentration parameter of the elastic fibers b_e was chosen to represent a nearly uniform fiber distribution, $b_\mathrm{e} = 0.01$. The numerical results for four different values of the degradation parameter ξ are shown in Fig. 5.

The Cauchy stress response decreases with the increase of the degradation parameter which is in good agreement with the structural observations described in Section 1. In addition, we investigated the influence of the number of discrete fiber directions m on the solution which is not shown here. It is obvious that a low number of discrete fiber directions is not able to represent the analytical result of the continuous model exactly. Therefore, the accuracy of the DFD model depends strongly on the discretization of the unit sphere. However, as described by Li et al. [46], the DFD model reduces the computational costs significantly when compared to the continuous approach, which is an important advantage of the DFD model. For example, the authors of [46] achieved a speed-up of 224 for a representative numerical example with 320 hexahedral elements by using the proposed DFD model. Other numerical examples or a different computer performance might undoubtedly change the speed-up downward or upward. Here,

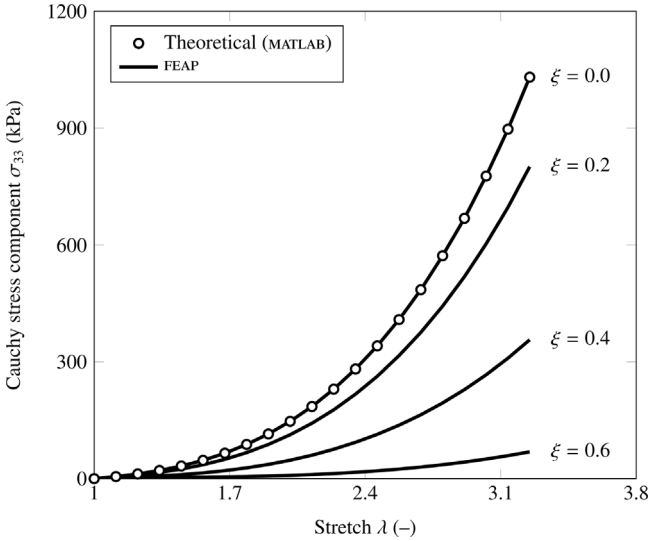

Fig. 5. Results of the uniaxial extension test with four different values for the degradation parameter ξ to demonstrate the effect of weakening in the radial direction. We chose the material parameters $c_1 = 56.59\,\text{kPa}$ and $c_2 = 3.83$ for the elastic fibers, and set the concentration parameter to $b_\text{e} = 0.01$ to describe a nearly uniform fiber dispersion. The results were obtained with a bulk modulus of $K = 8.0 \cdot 10^5$.

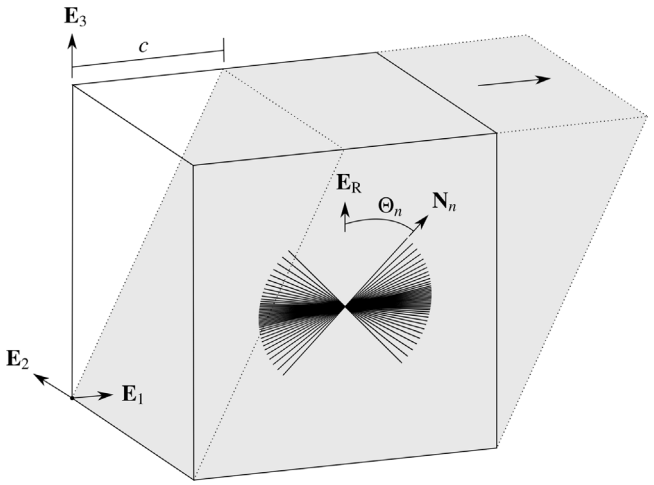

Fig. 6. Reference and intermediate configurations of a unit cube with a rotationally symmetric dispersion of elastic fibers at simple shear. The radial vector $\mathbf{E}_\text{R}$ is aligned with the $\mathbf{E}_3$-direction in the reference configuration. On the $(\mathbf{E}_1, \mathbf{E}_3)$-plane the cross-section of the 3D fiber dispersion including an arbitrary fiber direction $\mathbf{N}_n$ is shown.

we have chosen $m = 4000$ for an accurate numerical solution which is reasonable for the computational cheap problem under discussion.

3.1.3. Simple shear

In this example, we apply a simple shear deformation to an incompressible unit cube in the $(\mathbf{E}_1, \mathbf{E}_3)$-plane with the geometry of $1 \times 1 \times 1\,\text{mm}$, which is discretized by a single hexahedral element, as illustrated in Fig. 6. Similarly to the previous section, the radial vector $\mathbf{E}_\text{R}$ is assumed to be aligned with the $\mathbf{E}_3$-direction in the reference configuration to depict a realistic material behavior based on the introduced structural investigation in Section 1. Boundary conditions are chosen such that all the nodes on the $(\mathbf{E}_1, \mathbf{E}_2)$-plane are constrained in all three translational degrees of freedom, and on the top face of the unit cube a horizontal displacement in the $\mathbf{E}_1$-direction is applied.

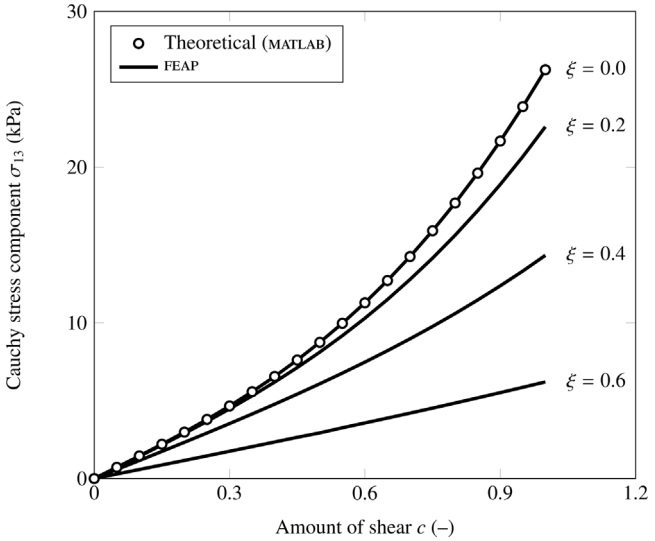

Fig. 7. Results of the shear test with four different values for the degradation parameter ξ (0, 0.2, 0.4, 0.6) to demonstrate the effect of weakening during shear deformation. We chose the material parameters $c_1 = 56.59$ kPa and $c_2 = 3.83$ for the elastic fibers, and set the concentration parameter to $b_e = 0.01$ to describe a nearly uniform fiber dispersion. The results were obtained with a bulk modulus of $K = 8.0 \cdot 10^5$.

Thus, for this particular case, we can formulate the deformation gradient in the matrix form as

$$[\mathbf{F}] = \begin{bmatrix} 1 & 0 & c \\ 0 & 1 & 0 \\ 0 & 0 & 1 \end{bmatrix}, \tag{44}$$

where c represents the amount of shear, and $I_4(\mathbf{N})$ is given in the explicit by

$$I_4(\Theta, \Phi) = 1 + c^2 \cos^2 \Theta + c \sin 2\Theta \cos \Phi. \tag{45}$$

In analogy to Li et al. [55], the Cauchy shear stress component σ_{13} in the $(\mathbf{E}_1, \mathbf{E}_2)$-plane is given by

$$\sigma_{13} = \alpha c + \gamma, \tag{46}$$

where the factors α and γ are defined over the domain $\Omega = \{(\Theta, \Phi) \in \mathbb{S}, I_4 > 1\}$ as

$$\alpha = \frac{c_1}{\pi} \int_\Omega \rho_e(\Theta, \Phi) I_4^{-1} (I_4^{c_2/2} - 1) \sin \Theta \cos^2 \Theta \mathrm{d}\Theta \mathrm{d}\Phi, \tag{47}$$

$$\gamma = \frac{c_1}{\pi} \int_\Omega \rho_e(\Theta, \Phi) I_4^{-1} (I_4^{c_2/2} - 1) \sin^2 \Theta \cos \Theta \cos \Phi \mathrm{d}\Theta \mathrm{d}\Phi. \tag{48}$$

Again, we verified the numerical results of the finite element solution with the analytical model in Matlab [60] using the same material and structural parameters for the constitutive model. Fig. 7 shows the Cauchy shear stress responses for four different values of the degradation parameter ξ. As shown, a decrease in the Cauchy shear stress response occurs when the degradation parameter increases which is in accordance with the results obtained previously, and the discussed structural observations of Section 1.

3.2. Computational study on an aortic dissection geometry motivated from patient data

The geometry of an acute aortic dissection, motivated from patient data, was reconstructed in Abaqus/Standard [48] to study the influence of radially-directed elastic fiber degradation on the stress distribution in an aortic dissection. We implemented the proposed model as a UMAT with a fully incompressible hybrid element formulation in Abaqus/Standard [48], and verified the model by comparing with previously obtained results of Section 3.1 and the numerical results published in the computational study of Li et al. [46].

Table 1
Constitutive parameters (μ, k_1, k_2, c_1, c_2) from the literature [61,67] and uniaxial extension tests from our laboratory. Structural parameters of the collagen fibers (α_c, b_c) are obtained from second-harmonic generation of human thoracic aortic tissues [65], while b_e is an assumed parameter.

Parameter	μ [kPa]	k_1 [kPa]	k_2 [–]	α_c [°]	b_c [–]	c_1 [kPa]	c_2 [–]	b_e [–]
Media	62.1	1.4	22.1	27.75 −27.19	5.75	56.59	3.83	0.01
Adventitia	21.6	1.4	22.1	55.21 −50.55	4.89	-	-	-

3.2.1. Identification of constitutive parameters

For the aortic dissection geometry we identified the material and structural parameters of the constitutive models by using experimental data documented in the literature, and from uniaxial extension testing results from our laboratory. The experimental results were obtained from a dissected human thoracic aortic sample of a 51-year-old male donor with high blood pressure including both medial and adventitial layers. The experimental protocol of the uniaxial extension test follows the description of Weisbecker et al. [64]. In short, the layers were separated from the surrounding tissue, and, subsequently, cut into a dog-bone shape specimen by using a metal template. To measure the displacement, two black markers were attached to the central region of the respective specimens. Then, the two specimens were preconditioned and subjected to uniaxial extension tests up to failure. To ensure an in vivo condition, all tests were carried out in a physiological bath at 37 °C. The displacement of the markers and the driven force data were recorded simultaneously. Following the results of the uniaxial extension test, we computed and, subsequently, plotted the Cauchy stress versus stretch curve.

The material parameters of the elastic fiber, i.e. $c_1 = 56.59\,\text{kPa}$ and $c_2 = 3.83$, were obtained from the results described in Section 3.1.1. In consequence of missing reliable experimental data, we chose a concentration parameter $b_e = 0.01$ which describes a nearly uniform fiber distribution of elastic fibers in the media. To investigate the influence of radially-directed elastic fibers, we compared a defined pathological condition ($\xi = 0.6$), with the healthy condition ($\xi = 0$). By applying the uniaxial extension testing results, we then fixed the material parameters of elastic fibers and, on the basis of the initial slope of the Cauchy stress versus stretch curve in the linear range, we approximated the shear modulus of the ground substance to be $\mu = 61.2\,\text{kPa}$ in the medial layer. For the adventitial layer, we neglected the presence of the elastic fibers. Hence, the shear modulus of the ground substance was used to approximate the initial slope of the Cauchy stress versus the stretch curve. We estimated a shear modulus of $\mu = 21.6\,\text{kPa}$. The obtained values are in accordance with previous studies [64].

Next, we utilized the results of Schriefl et al. [65] which investigate, inter alia, the structural parameters of collagen fiber in the human thoracic aorta. After image analyses, the authors identified the layer-specific 3D fiber dispersion of two families of collagen fibers via second-harmonic generation. The mean fiber orientation of the two families of collagen fibers are specified by the angle α_c, which is defined in the $(\mathbf{E}_1, \mathbf{E}_2)$-plane as the angle between the circumferential direction $\mathbf{E}_1$ and the respective mean fiber direction, see Fig. 8. The fitting procedure of the image data with a von Mises distribution provided a concentration parameter of the media, $b_c = 5.75$, and the adventitia, $b_c = 4.89$, for both fiber families. Unfortunately, we were not able to obtain any experimental data for the structural parameters of dissected human tissues. For the DFD model, the PDF was discretized over the unit hemisphere with $m = 640$ triangles, which reduces the computational costs, while still providing a good accuracy. We used the same discretization for collagen and elastic fibers. Next, we specified the single collagen fiber strain–energy function $f_c(\bar{I}_4)$ in the exponential form [66] as

$$f_c(\bar{I}_4) = \frac{k_1}{2k_2}\{\exp[k_2(\bar{I}_4 - 1)^2] - 1\}, \tag{49}$$

with the collagen fiber stiffness k_1, a positive material parameter with the dimension of stress, and the collagen fiber shape parameter k_2, a positive material parameter with no dimension. We identified the material parameters of collagen fibers according to the experimental data of Enea et al. [67]. Finally, the material and structural parameters of the medial and adventitial layers are summarized in Table 1. Due to missing reliable data we set the recruitment stretch of collagen fibers to $\lambda_{cr} = 1$.

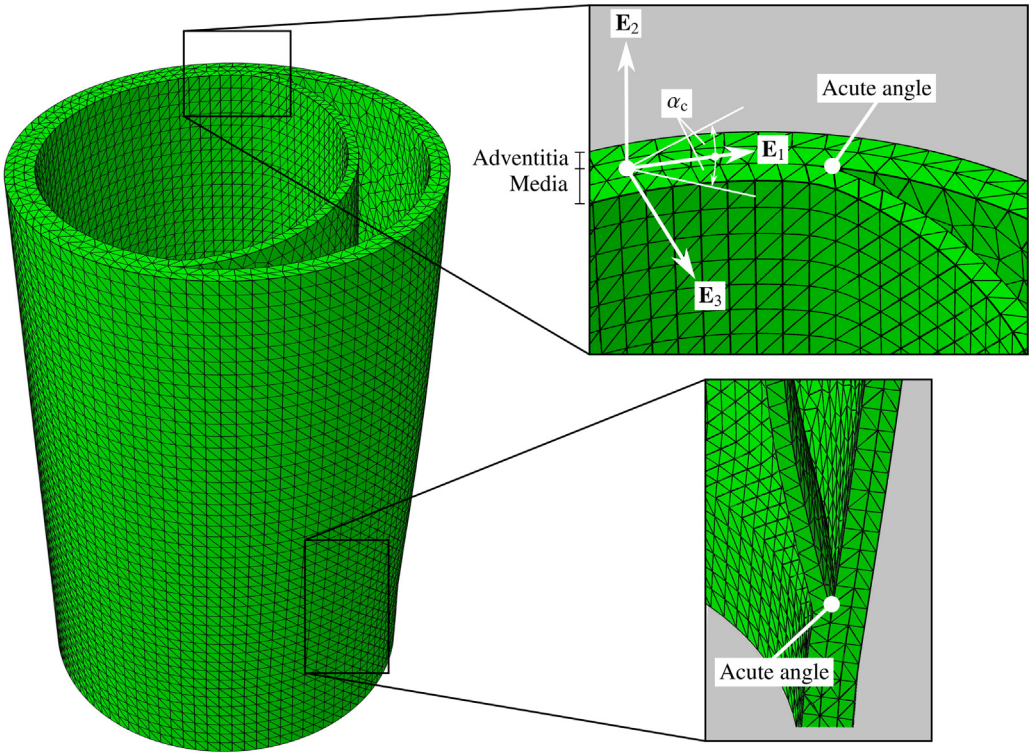

Fig. 8. Reconstructed geometry of an acute aortic dissection, motivated from patient data, with two layers (media and adventitia), and the presence of an acute angle characterizing the dissection. Each layer was discretized in Abaqus/Standard [48] with 10-node quadratic tetrahedral elements (C3D10H) individually, in total 78 389 elements were used for the finite element analysis.

3.2.2. Aortic dissection geometry and mesh

Fig. 8 illustrates the geometry of an acute aortic dissection, a geometrical setting motivated by patient data. A section of the descending thoracic aorta has a length of 35 mm, and the aortic wall is composed of two distinct layers, i.e. media and adventitia. The experimental study of Amabili et al. [68] provides data of layer-specific thickness measurements which were used to define the dimensions of the aortic wall. The thickness of the media (0.91 mm) and the adventitia (0.49 mm) are based on the results of a 67-year-old donor. Here, we neglected the intima so that its thickness (0.21 mm) was added to the media. We further assumed that the false lumen initiates halfway of the media. The true and false lumina are characterized by either a circular or an elliptical shape which is based on the observation of various studies [69,70]. From the experimental results of Amabili et al. [68], the inner diameter of the true lumen on the bottom of the geometry is set to 19.58 mm. The inner diameter of the true lumen and the thickness of the aortic wall originate both from the measurement results of the same donor. Note that the shape of the true lumen varies from the bottom to the top due to the development of the false lumen. Moreover, we assumed the presence of an 'acute angle', which is a characteristic angle in acute aortic dissection between the dissection flap and the outer wall of the false lumen [71,72]. In chronic aortic dissection, the acute angle is often not visible due to neointimal growth and local thrombosis.

Then, Abaqus/Standard [48] was used to discretize the geometry with 78 389 10-node quadratic tetrahedral elements (C3D10H) applying a hybrid formulation to ensure incompressibility. The mesh quality was verified and a local coordinate system was constructed using Abaqus/Standard [48] by defining a discrete coordinate system for each layer. We set the $\mathbf{E}_1$-direction as the circumferential direction (clockwise) and the $\mathbf{E}_3$-direction as the radial direction pointing in the direction of the respective lumen, as shown in Fig. 8. Consequently, the $\mathbf{E}_2$-direction represents the longitudinal direction.

3.2.3. Applied boundary conditions

A displacement boundary condition is applied at the bottom face of the model to impose an axial prestretch of $\lambda = 1.07$, which is based on 55.5 to 66-year-old donors [73]. This is in accordance with the previously chosen dimensions of the aortic wall, the inner diameter and the thickness of the aortic wall. In addition, we applied a static internal pressure of 75 mmHg (and 117 mmHg) in the false lumen and 72 mmHg (and 120 mmHg) in the true lumen to simulate the blood pressure in diastole (and systole) [74]. The static internal pressure models the presence of blood in the aortic wall, which we assumed to be constant over the rather short length of the geometry (35 mm). Moreover, we did not consider wall shear stresses, because the magnitude of wall shear stresses in the aorta, which is usually < 10 Pa [74], is negligibly small in comparison to mechanical stresses in the aortic wall. A direct impact of wall shear stresses on the mechanical stress distribution in the aortic wall can therefore be excluded. For the sake of completeness, we neglected thrombus formation in the false lumen which may influence the blood pressure. To eliminate the rigid body motion, the top face of the model geometry is restricted in the axial direction, and a single point located at the top face is restricted in the $\mathbf{E}_1$-direction and another in the $(\mathbf{E}_1, \mathbf{E}_2)$-plane.

3.2.4. Numerical results

We constructed the finite element model for the quasi-static boundary-value problem in Abaqus/Standard [48] and solved it by using the quasi-Newton method with a constant damping factor of $1 \cdot 10^{-3}$, which was estimated by trial and error. The simulations were performed with an automatic time incrementation. We chose an initial time increment of $\tau = 1 \cdot 10^{-3}$ which decreases to a minimum incremental size of $\tau_{\min} = 5 \cdot 10^{-7}$, whenever numerical instabilities occurred. The numerical simulation was completed in about 90 min on a Windows computer with an Intel Xeon W-2145, 8C/16T, $3.70 - 4.50$ GHz processor and 64 GB of memory.

Fig. 9 illustrates the computational results for the healthy condition by showing the maximum principal stresses in the false and true lumina at diastole and systole. Here the results of the pathological condition did not significantly differ from the healthy condition. In diastole, the applied pressure in the false lumen, 75 mmHg, is slightly higher than that in the true lumen, 72 mmHg, which causes the dissection flap to bend towards the true lumen. Furthermore, the maximum principal stress in the outer wall of the false lumen is significantly higher than that in the outer wall of the true lumen which can be explained by the decreased wall thickness. Moreover, the peak stress is located at the acute angle, at the lateral side to the false lumen. It appears that the stress concentrations are caused by the dilatation of the two lumina, which, in consequence, pulls the dissection flap almost orthogonal from the outer wall. In comparison, the higher pressure in the systole leads to a more pronounced dilatation of the outer aortic wall, which therefore leads to even higher stresses. Subsequently, a progression of the false lumen may be more likely in the systole. Fig. 9 displays also evaluated computed tomography (CT) images at the end of the aortic arch which display the minimal and maximal extents of the false and true lumina over the cardiac cycle, taken from the study of Ganten et al. [69]. The minimal and maximal extents of the true lumen correspond approximately with the systole and diastole, respectively. However, the shape and geometry of the two lumina in the CT image are slightly different from the created geometry due to differences in the pressure and the geometry.

The influence of the degraded elastic fibers on promoting the progression of the false lumen can neither be shown nor refuted by this example. Considering the chosen example, the degradation of radially-directed elastic fibers do not alter the stress state significantly in the domain around the acute angle.

4. Discussion

In this study, we proposed a novel application of the DFD model for characterizing the symmetrically dispersed elastic fibers in the aortic wall, as previously discussed [45]. The discrete approach allows us to simulate the degradation of radially-directed inter-lamellar elastic fibers, which is related to the pathology of aortic dissections. According to previous studies [46,52], we formulated the strain–energy function of elastic fibers by means of the DFD model and, subsequently, introduced a degradation parameter to exclude degraded elastic fibers from the strain–energy function. The obtained constitutive model of elastic fibers then depends only on the fibers under tension and a single degradation parameter.

Next, we presented the decoupled form of the strain–energy function into volumetric and isochoric parts which is based on the multiplicative decomposition of the deformation gradient. Furthermore, the isochoric part was additively decomposed into the constituents of the aortic wall, namely the ground substance, collagen fibers and elastic fibers. The continuum mechanical framework also included the explicit expressions of the Cauchy stress

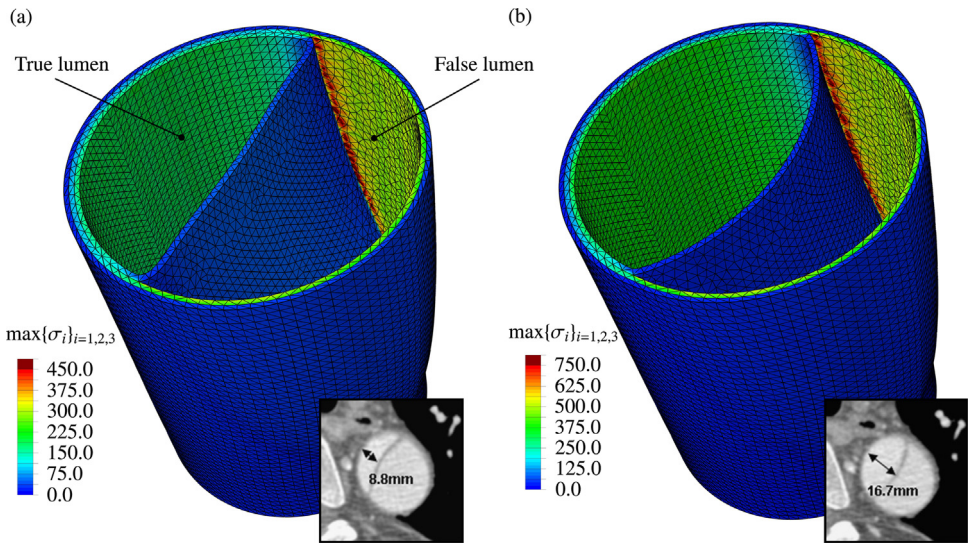

Fig. 9. Computational results of the finite element analysis illustrating the maximal principal stresses in the false and true lumina at (a) diastole and (b) systole with $\xi = 0.6$ in comparison with evaluated CT images at the end of the aortic arch, which display the minimal and maximal extents of the false and true lumina over the cardiac cycle.
Source: CT images were reprinted from Ganten et al. [69].

tensor and the elasticity tensor in the decoupled form. The constitutive model was then implemented in the finite element analysis program FEAP to demonstrate the performance of the model with two numerical examples, uniaxial tension and simple shear. The results were in good agreement with the analytical solution computed in Matlab, and showed the expected weakening of the medial layer with respect to delamination and shear loads.

Subsequently, we implemented the constitutive model as a UMAT in Abaqus/Standard. The geometry of an acute aortic dissection, motivated from patient data, was then created in Abaqus/Standard and (physiological) boundary conditions were applied to compute the deformation and stress distribution of the dissected aortic wall under two quasi-static pressure states in the cardiac cycle, systole and diastole. The computational results provided meaningful insights in the stress distribution of the dissected aortic wall. The magnitude of the stress distribution is approximately in line with other computational investigations [33], however, it is strongly depended on the chosen material parameters which differ from patient to patient. As noted before, the effect of the degradation of elastic fibers in the radial direction were invisible in the numerical example which can be explained on the basis of different reasons. Firstly, the stiffness contribution of the elastic fibers may have only a limited influence on the stress distribution at higher pressures because the majority of the load is borne by the collagen fibers. This is also supported by the recently published results of Wang et al. [44]. However, the decrease in the radial stiffness leads to a lowering of the failure stress of the tissues, which promotes the progression of a dissection. To include a fracture criterion into the model and to further analyze this particular example is a next meaningful step. Secondly, there may be too many collagen fibers specified between the lamellae due to the defined rotationally symmetric fiber dispersion function. This dispersion function implies that many collagen fibers are oriented radially, which may not be the case in reality. Therefore, we motivate future studies to better investigate structural and mechanical properties of dissected human aortic tissue, so that computational results on aortic dissection geometries are more meaningful. A review on experimental investigations on the aortic wall failure properties with the focus on dissection was recently published by Sherifova and Holzapfel [75]. Thirdly, adaptive finite element methods should be used with the purpose to create an optimal mesh with minimum degrees of freedom. Stress gradients could then be better captured, i.e. regions with higher gradients of stress field produce then lower values of estimated error. Finally, the aortic wall is primarily subjected to a stretch in the circumferential direction caused by the inflation of the vessel due to blood pressure. As a consequence, the aortic wall becomes thinner which then compresses the lamellar units of the media. The inter-lamellar elastic fibers are not able to bear loads under compression, so that they do not contribute to the stiffness of the aortic wall under this conditions. Therefore, it is plausible that the macroscopic effects of the degradation of elastic fibers are invisible in this particular boundary-value problem.

The computational simulation of the aortic model was mainly performed under static loading conditions in the false and the true lumen. The pulsating blood pressure causes a pressure difference between the false and true lumina which is assumed to be between 2–4 mmHg [74,76]. This comparatively low pressure difference suggests that the interchange of blood between the true and false lumina is also fairly low. Hence, high velocities of the blood flow are only expected in the region proximal to the intimal tear, and a dissection progression, induced by blood jetting into the acute angle, seems rather unlikely. This is somehow in contradiction to previous discussion in [33]. Nevertheless, the pressure differences may alter with the location and characteristic of the entry tear, and possible reentry tears [74,77]. On the contrary, our computational results suggest that the medial layer is delaminated by the stretch applied to the dissection flap. The dissection flap is stretched due to the cyclic dilatation of the false and true lumina, and, subsequently, pulled apart from the remaining medial layer. This may promote the progression of the false lumen. In addition, hypertension and age-related dilatation of the aortic wall, known as risk factors for aortic dissection, may increase the applied stretch on the dissection flap even more.

The dissection flap is exposed to a cyclic movement which is caused by the alternating pressure gradient between the false and true lumina, as shown in Fig. 9. This movement decreases with the progression of the aortic dissection due to stiffening of the dissection flap, as suggested by some studies [69,70,78]. The stiffening of the dissection flap is the result of remodeling, or more precisely fibrosis, which stiffens the dissection flap, and thus limits the movement during the cardiac cycle. The stiffening may alter the stress distribution in the dissection flap and, therefore, may also increase the stress concentration at the acute angle significantly. To the best of the authors' knowledge the computational study of Bäumler et al. [76] incorporated the remodeling of the dissection flap at the very first. Future studies incorporating the dynamic movement of the dissection flap, as well as the ongoing fibrosis, may provide more accurate results. Both processes may impact the progression of the false lumen.

The progression of the false lumen may also be influenced by the contraction of SMCs. SMCs align primarily with the circumferential direction, but they show a radial tilt in the medial layer [15]. In consequence, they can contribute to the radial strength of the medial layer [79,80]. As mentioned earlier, dysfunction and apoptosis of SMC are strongly associated with aortic dissection. However, there are just a few computational studies incorporating dysfunction and apoptosis of SMCs in association with aortic dissection [25,26]. Thus, there is still a need of quantifying the impact of the active constrictions of SMCs on the delamination strength in the aortic wall both from the experimental and the computational point of view.

In summary, we presented a constitutive approach to model the elastic fibers in the medial layer by using the DFD model, and showed the importance of modeling degraded elastic fibers with respect to aortic dissection. Furthermore, we specified possible mechanisms promoting the progression of the false lumen, since there may be multiple triggers, and, in this regard, we discussed possible directions of future computational studies associated with aortic dissection.

Declaration of competing interest

The authors declare that they have no known competing financial interests or personal relationships that could have appeared to influence the work reported in this paper.

Acknowledgments

This work was partly funded by Graz University of Technology, Austria, through the LEAD Project on the 'Mechanics, Modeling, and Simulation of Aortic Dissection'. We thank Dr. Jeremi K. Mizerski (Otto von Guericke University Magdeburg, Germany and Samodzielny Publiczny Szpital Wojewódzki im. Papieża Jana Pawła II w Zamościu, Zamość, Poland) for the discussions related to aortic dissections, and Selda Sherifova (Graz University of Technology, Austria) for providing uniaxial extension test results of a dissected human thoracic aorta.

References

[1] F. Nicholls, Observations concerning the body of His Late Majesty, October 26, 1760, Phil. Trans. 52 (1761) 265–275.
[2] F.J. Criado, Aortic dissection: a 250-year perspective, Tex Heart Inst. J. 38 (6) (2011) 694–700.
[3] J. Erdheim, Medionecrosis aortae idiopathica, Virch. Arch. Pathol. Anat. 273 (1929) 454–479.
[4] J. Erdheim, Medionecrosis aortae idiopathica cystica, Virch. Arch. Pathol. Anat. 276 (1930) 187–229.
[5] E. Girdauskas, T. Kuntze, M.A. Borger, T. Doenst, M. Mochalski, T. Walther, V. Falk, F.W. Mohr, Long-term prognosis of type a aortic dissection in non-Marfan patients with histologic pattern of cystic medial necrosis, Ann. Thorac. Surg. 85 (3) (2008) 972–977.

[6] I.B. Alomari, Y.S. Hamirani, G. Madera, C. Tabe, N. Akhtar, V. Raizada, Aortic intramural hematoma and its complications, Circulation 129 (6) (2014) 711–716.
[7] C. Nienaber, R. Clough, N. Sakalihasan, T. Suzuki, R. Gibbs, F. Mussa, M. Jenkins, M. Thompson, A. Evangelista, J. Yeh, N. Cheshire, U. Rosendahl, J. Pepper, Aortic dissection, Nat. Rev. Dis. Primers 2 (2016) 16053.
[8] J.D. Humphrey, Possible mechanical roles of glycosaminoglycans in thoracic aortic dissection and associations with dysregulated transforming growth factor-β, J. Vasc. Res. 50 (1) (2013) 1–10.
[9] T.J.M. Schlatmann, A.E. Becker, Histologic changes in the normal aging aorta: implications for dissecting aortic aneurysm, Am. J. Cardiol. 39 (1) (1977) 13–20.
[10] T.J.M. Schlatmann, A.E. Becker, Pathogenesis of dissecting aneurysm of aorta: comparative histopathologic study of significance of medial changes, Am. J. Cardiol. 39 (1) (1977) 21–26.
[11] E.W. Larson, W.D. Edwards, Risk factors for aortic dissection: a necropsy study of 161 cases, Am. J. Cardiol. 53 (6) (1984) 849–855.
[12] P.W. Fedak, S. Verma, T.E. David, R.L. Leask, R.D. Weisel, J. Butany, Clinical and pathophysiological implications of a bicuspid aortic valve, Circulation 106 (8) (2002) 900–904.
[13] D.G. Guzzardi, A.J. Barker, P. van Ooij, S.C. Malaisrie, J.J. Puthumana, D.D. Belke, H.E. Mewhort, D.A. Svystonyuk, S. Kang, S. Verma, J. Collins, J. Carr, R.O. Bonow, M. Markl, J.D. Thomas, P.M. McCarthy, P.W. Fedak, Valve-related hemodynamics mediate human bicuspid aortopathy: insights from wall shear stress mapping, J. Am. Coll. Cardiol. 66 (8) (2015) 892–900.
[14] R.A. Levine, A.A. Hagège, D.P. Judge, M. Padala, J.P. Dal-Bianco, E. Aikawa, J. Beaudoin, J. Bischoff, N. Bouatia-Naji, P. Bruneval, J.T. Butcher, A. Carpentier, M. Chaput, A.H. Chester, C. Clusel, F.N. Delling, H.C. Dietz, C. Dina, R. Durst, F.-F. L., H.M. D., M. Jensen, X.P. Jeunemaitre, H. Le Marec, T. Le Tourneau, R.R. Markwald, J. Mérot, E. Messas, D.P. Milan, T. Neri, R.A. Norris, D. Peal, M. Perrocheau, V. Probst, M. Pucéat, N. Rosenthal, J. Solis, S.J. J., E. Schwammenthal, S.A. Slaugenhaupt, J.K. Song, M.H. Yacoub, Mitral valve disease–morphology and mechanisms, Nat. Rev. Cardiol. 12 (12) (2015) 689–710.
[15] K.P. Dingemans, P. Teeling, J.H. Lagendijk, A.E. Becker, Extracellular matrix of the human aortic media: an ultrastructural histochemical and immunohistochemical study of the adult aortic media, Anat. Rec. 258 (1) (2000) 1–14.
[16] M.K. O'Connell, S. Murthy, S. Phan, C. Xu, J. Buchanan, R. Spilker, R.L. Dalman, C.K. Zarins, W. Denk, C.A. Taylor, The three-dimensional micro- and nanostructure of the aortic medial lamellar unit measured using 3D confocal and electron microscopy imaging, Matrix Biol. 27 (3) (2008) 171–181.
[17] K.S. Midwood, J.E. Schwarzbauer, Elastic fibers: building bridges between cells and their matrix, Curr. Biol. 12 (8) (2002) R279–R281.
[18] Y. Nakashima, T. Kurozumi, K. Sueishi, K. Tanaka, Dissecting aneurysm: a clinicopathologic and histopathologic study of 111 autopsied cases, Hum. Pathol. 21 (3) (1990) 291–296.
[19] N.F. MacLean, N.L. Dudek, M.R. Roach, The role of radial elastic properties in the development of aortic dissections, J. Vasc. Surg. 29 (4) (1999) 703–710.
[20] Y. Nakashima, Pathophysiology of aortic dissection and abdominal aortic aneurysm, in: S. Kawada, T. Ueda, H. Shimizu (Eds.), Cardio-Aortic and Aortic Surgery, Keio University International Symposia for Life Sciences and Medicine, Springer, Tokyo, 2001, pp. 4–11.
[21] Y. Nakashima, Pathogenesis of aortic dissection: elastic fiber abnormalities and aortic medial weakness, Ann. Vasc. Dis. 3 (1) (2010) 28–36.
[22] F.S. Cikach, C.D. Koch, T.J. Mead, J. Galatioto, B.B. Willard, K.B. Emerton, M.J. Eagleton, E.H. Blackstone, F. Ramirez, E.E. Roselli, S.S. Apte, Massive aggrecan and versican accumulation in thoracic aortic aneurysm and dissection, JCI Insight 3 (5) (2018).
[23] S. Roccabianca, G.A. Ateshian, J.D. Humphrey, Biomechanical roles of medial pooling of glycosaminoglycans in thoracic aortic dissection, Biomech. Model. Mechanobiol. 13 (1) (2014) 13–25.
[24] S. Roccabianca, C. Bellini, J.D. Humphrey, Computational modelling suggests good, bad and ugly roles of glycosaminoglycans in arterial wall mechanics and mechanobiology, J. R. Soc. Interface 11 (97) (2014) 20140397.
[25] H. Ahmadzadeh, M.K. Rausch, J.D. Humphrey, Particle-based computational modelling of arterial disease, J. R. Soc. Interface 15 (149) (2018) 20180616.
[26] H. Ahmadzadeh, M. Rausch, J.D. Humphrey, Modeling lamellar disruption within the aortic wall using a particle-based approach, Sci. Rep. 9 (2019) 15320.
[27] T.C. Gasser, G.A. Holzapfel, Modeling the propagation of arterial dissection, Eur. J. Mech. A-Solid 25 (4) (2006) 617–633.
[28] A. Ferrara, A. Pandolfi, A numerical study of arterial media dissection processes, Int. J. Fract. 166 (2010) 21–33.
[29] A. Ferrara, A. Pandolfi, Numerical modelling of fracture in human arteries, Comput. Methods Biomech. Biomed. Eng. 11 (5) (2008) 553–567.
[30] L. Wang, S.M. Roper, X.Y. Luo, N.A. Hill, Modelling of tear propagation and arrest in fibre-reinforced soft tissue subject to internal pressure, J. Eng. Math. 95 (1) (2015) 249–265.
[31] L. Wang, S.M. Roper, N.A. Hill, X. Luo, Propagation of dissection in a residually-stressed artery model, Biomech. Model. Mechanobiol. 16 (1) (2017) 139–149.
[32] L. Wang, N.A. Hill, S.M. Roper, X. Luo, Modelling peeling- and pressure-driven propagation of arterial dissection, J. Eng. Math. 109 (1) (2018) 227–238.
[33] O. Gültekin, S.P. Hager, H. Dal, G.A. Holzapfel, Computational modeling of progressive damage and rupture in fibrous biological tissues: application to aortic dissection, Biomech. Model. Mechanobiol. 18 (2019) 1607–1628.
[34] G.A. Holzapfel, B. Fereidoonnezhad, Modeling of damage in soft biological tissues. hyperelastic constitutive laws for finite element modeling, in: Y. Payan, J. Ohayon (Eds.), Biomechanics of Living Organs, Academic Press, New York, 2017, pp. 101–123.
[35] O. Gültekin, G.A. Holzapfel, A brief review on computational modeling of rupture in soft biological tissues. computational methods in applied sciences, in: O. Oñate, D. Peric, E. de Souza Neto, E. Chiumenti (Eds.), Advances in Computational Plasticity. A Book in Honour of D. Roger J. Owen, Vol. 46, Springer Nature, 2018, pp. 113–144.

[36] O. Gültekin, H. Dal, G.A. Holzapfel, Numerical aspects of anisotropic failure in soft biological tissues favor energy-based criteria: a rate-dependent anisotropic crack phase-field model, Comput. Methods Appl. Mech. Engrg. 331 (2018) 23–52.
[37] S.B. Shah, C. Witzenburg, F.M. Hadi, H.P. Wagner, J.M. Goodrich, P. Alford, V.H. Barocas, Prefailure and failure mechanics of the porcine ascending thoracic aorta: experiments and a multiscale model, J. Biomech. Eng. 136 (2) (2014).
[38] C. Witzenburg, R. Y. Dhume, S.B. Shah, C. Korenczuk, H.P. Wagner, P. Alford, V.H. Barocas, Failure of the porcine ascending aorta: multidirectional experiments and a unifying microstructural model, J. Biomech. Eng. 139 (3) (2016).
[39] J.R. Thunes, S. Pal, R.N. Fortunato, J.A. Phillippi, T.G. Gleason, D.A. Vorp, S. Maiti, A structural finite element model for lamellar unit of aortic media indicates heterogeneous stress field after collagen recruitment, J. Biomech. 49 (9) (2016) 1562–1569.
[40] J.R. Thunes, J.A. Phillippi, T.G. Gleason, D.A. Vorp, S. Maiti, Structural modeling reveals microstructure-strength relationship for human ascending thoracic aorta, J. Biomech. 71 (2018) 84–93.
[41] S. Pal, A. Tsamis, S. Pasta, A. D'Amore, T.G. Gleason, D.A. Vorp, S. Maiti, A mechanistic model on the role of "radially-running" collagen fibers on dissection properties of human ascending thoracic aorta, J. Biomech. 47 (5) (2014) 981–988.
[42] S. Pasta, J.A. Phillippi, T.G. Gleason, D.A. Vorp, Effect of aneurysm on the mechanical dissection properties of the human ascending thoracic aorta, J. Thorac. Cardiovasc. Surg. 143 (2) (2012) 460–467.
[43] X. Yu, B. Suki, Y. Zhang, Avalanches and power law behavior in aortic dissection propagation, Sci. Adv. 6 (21) (2020).
[44] R. Wang, X. Yu, Y. Zhang, Mechanical and structural contribution of elastin and collagen fibers to interlamellar bonding in the arterial wall, Biomech. Model. Mechanobiol. (2020).
[45] G.A. Holzapfel, R.W. Ogden, S. Sherifova, On fibre dispersion modelling of soft biological tissues: a review, Proc. Math. Phys. Eng. Sci. 475 (2224) (2019) 20180736.
[46] K. Li, R.W. Ogden, G.A. Holzapfel, A discrete fibre dispersion method for excluding fibres under compression in the modelling of fibrous tissues, J. R. Soc. Interface 15 (138) (2018) 20170766.
[47] R.L. Taylor, FEAP – A Finite Element Analysis Program, Version 8.5 User Manual, University of California, Berkeley, 2017.
[48] ABAQUS/Standard User's Manual, Version 2017, Dassault Systèmes Simulia Corporation, Johnston, RI, USA, 2017.
[49] P.J. Flory, Thermodynamic relations for highly elastic materials, Trans. Faraday Soc. 57 (1961) 829–838.
[50] R.W. Ogden, Nearly isochoric elastic deformations: application to rubberlike solids, J. Mech. Phys. Solids 26 (1) (1978) 37–57.
[51] G.A. Holzapfel, Nonlinear Solid Mechanics. A Continuum Approach for Engineering, John Wiley & Sons, Chichester, 2000.
[52] K. Li, G.A. Holzapfel, Multiscale modeling of fiber recruitment and damage with a discrete fiber dispersion method, J. Mech. Phys. Solids 126 (2019) 226–244.
[53] M.A. Lillie, J.M. Gosline, Tensile residual strains on the elastic lamellae along the porcine thoracic aorta, J. Vasc. Res. 43 (2006) 587–601.
[54] S. Sugita, T. Matsumoto, Multiphoton microscopy observations of 3D elastin and collagen fiber microstructure changes during pressurization in aortic media, Biomech. Model. Mechanobiol. 16 (3) (2017) 763–773.
[55] K. Li, R.W. Ogden, G.A. Holzapfel, An exponential constitutive model excluding fibres under compression: application to extension–inflation of a residually stressed carotid artery, Math. Mech. Solids 23 (8) (2018) 1206–1224.
[56] M.R. Hill, X. Duan, G.A. Gibson, S. Watkins, A.M. Robertson, A theoretical and non-destructive experimental approach for direct inclusion of measured collagen orientation and recruitment into mechanical models of the artery wall, J. Biomech. 45 (5) (2012) 762–771.
[57] H. Weisbecker, M.J. Unterberger, G.A. Holzapfel, Constitutive modelling of arteries considering fibre recruitment and three-dimensional fibre distribution, J. R. Soc. Interface 12 (105) (2015) 20150111.
[58] T.C. Gasser, R.W. Ogden, G.A. Holzapfel, Hyperelastic modelling of arterial layers with distributed collagen fibre orientations, J. R. Soc. Interface 3 (6) (2006) 15–35.
[59] J.C. Simo, R.L. Taylor, Quasi-incompressible finite elasticity in principal stretches. continuum basis and numerical algorithms, Comput. Methods Appl. Mech. Engrg. 85 (3) (1991) 273–310.
[60] MATLAB, The MathWorks Inc., Natick, MA, USA, 2018.
[61] K. Tanishita, K. Yamamoto (Eds.), Vascular Engineering: New Prospects of Vascular Medicine and Biology with a Multidiscipline Approach, Springer Japan, 2016.
[62] B. Markert, W. Ehlers, N. Karajan, A general polyconvex strain-energy function for fiber-reinforced materials, PAMM 5 (2005) 245–246.
[63] K. Li, R.W. Ogden, G.A. Holzapfel, Computational method for excluding fibers under compression in modeling soft fibrous solids, Eur. J. Mech. A-Solid 57 (2016) 178–193.
[64] H. Weisbecker, C. Viertler, D.M. Pierce, G.A. Holzapfel, The role of elastin and collagen in the softening behavior of the human thoracic aortic media, J. Biomech. 46 (11) (2013) 1859–1865.
[65] A.J. Schriefl, G. Zeindlinger, D.M. Pierce, P. Regitnig, G.A. Holzapfel, Determination of the layer-specific distributed collagen fibre orientations in human thoracic and abdominal aortas and common iliac arteries, J. R. Soc. Interface 9 (71) (2012) 1275–1286.
[66] G.A. Holzapfel, T.C. Gasser, R.W. Ogden, A new constitutive framework for arterial wall mechanics and a comparative study of material models, J. Elasticity 61 (1) (2000) 1–48.
[67] D. Enea, F. Henson, S. Kew, J. Wardale, A. Getgood, R. Brooks, N. Rushton, Extruded collagen fibres for tissue engineering applications: effect of crosslinking method on mechanical and biological properties, J. Mater. Sci. Mater. Med. 22 (2011) 1569–1578.
[68] M. Amabili, P. Balasubramanian, I. Bozzo, I.D. Breslavsky, G. Ferrari, Layer-specific hyperelastic and viscoelastic characterization of human descending thoracic aortas, J. Mech. Behav. Biomed. Mater. 99 (2019) 27–46.
[69] M.-K. Ganten, T.F. Weber, H. von Tengg-Kobligk, D. Böckler, W. Stiller, P. Geisbüsch, G.W. Kauffmann, S. Delorme, M. Bock, H.-U. Kauczor, Motion characterization of aortic wall and intimal flap by ECG-gated CT in patients with chronic b-dissection, Eur. J. Radiol. 72 (1) (2009) 146–153.

[70] S. Peterss, A.M. Mansour, J.A. Ross, I. Vaitkeviciute, P. Charilaou, J. Dumfarth, H. Fang, B.A. Ziganshin, J.A. Rizzo, A.J. Adeniran, J.A. Elefteriades, Changing pathology of the thoracic aorta from acute to chronic dissection: literature review and insights, J. Am. Coll. Cardiol. 68 (10) (2016) 1054–1065.
[71] D.M. Williams, J.C. Andrews, M.V. Marx, G.D. Abrams, Creation of reentry tears in aortic dissection by means of percutaneous balloon fenestration: gross anatomic and histologic considerations, J. Vasc. Interv. Radiol. 4 (1) (1993) 75–83.
[72] D.Y. Lee, D.M. Williams, G.D. Abrams, The dissected aorta: part II. Differentiation of the true from the false lumen with intravascular US, Radiology 32 (1) (1997) 32–36.
[73] L. Horný, T. Adamek, M. Kulvajtova, Analysis of axial prestretch in the abdominal aorta with reference to post mortem interval and degree of atherosclerosis, J. Mech. Behav. Biomed. Mater. 33 (2014) 93–98.
[74] S. Pirola, B. Guo, C. Menichini, S. Saitta, W. Fu, Z. Dong, X. Xu, 4D flow MRI-based computational analysis of blood flow in patient-specific aortic dissection, IEEE Trans. Biomed. Eng. 66 (2019) 3411–3419.
[75] S. Sherifova, G.A. Holzapfel, Biomechanics of aortic wall failure with a focus on dissection and aneurysm: a review, Acta Biomater. 99 (2019) 1–17.
[76] K. Bäumler, V. Vedula, A.M. Sailer, J. Seo, P. Chiu, G. Mistelbauer, F.P. Chan, M.P. Fischbein, A.L. Marsden, D. Fleischmann, Fluid–structure interaction simulations of patient-specific aortic dissection, Biomech. Model. Mechanobiol. (2020).
[77] T.T. Tsai, A. Evangelista, C.A. Nienaber, T. Myrmel, G. Meinhardt, J.V. Cooper, D.E. Smith, T. Suzuki, R. Fattori, A. Llovet, J. Froehlich, S. Hutchison, A. Distante, T. Sundt, J. Beckman, J.L. Januzzi, E.M. Isselbacher, K.A. Eagle, Partial thrombosis of the false lumen in patients with acute type b aortic dissection, New Engl. J. Med. 357 (4) (2007) 349–359.
[78] H. Minami, T. Sugimoto, M. Okada, Evaluation of acute aortic dissection by cine-MRI, Kobe J. Med. Sci. 45 (1) (1999) 1–11.
[79] J.M. Clark, S. Glagov, Structural integration of the arterial wall. I. Relationships and attachments of medial smooth muscle cells in normally distended and hyperdistended aortas, Lab. Invest. 40 5 (1979) 587–602.
[80] M.W. Carson, M.R. Roach, The strength of the aortic media and its role in the propagation of aortic dissection, J. Biomech. 23 (6) (1990) 579–588.